Characterization of internal quality factors in surface-treated and deep-etched superconducting CPW resonators

Kian van der Enden

Bachelor's Thesis

Quantum Transport Group

Kavli Institute of Nanoscience

Delft University of Technology

Delft, The Netherlands

June 14, 2014

BEP Advisors: dr.ing. Alessandro Bruno, dr.ir. Gijs de Lange and dr. Leonardo DiCarlo

Author: Kian van der Enden

Characterization of internal quality factors in surface-treated and deep-etched superconducting CPW resonators

Abstract

For quantum computing with superconducting qubits, fabricating transmon qubits with increased coherence time is crucial, especially in view of multi-qubit quantum processors. The fabrication process, geometries and materials used to fabricate a transmon qubit are similar to the fabrication of CPW resonators. However, due to shorter fabrication time and straightforward measurement scheme of the latter, finding a way to increase the internal quality factor Q_i in a CPW resonator is a quick way to gain insight into methods to increase the coherence time of a transmon qubit. The main goal of this research is to characterize the Q_i at cryogenic temperature and single photon level of CPW resonators that are fabricated with novel surface treatments and etching techniques. The highest Q_i is observed for resonators etched using Deep Reactive Ion Etching and HDMS surface treatment, which reached $\sim 2 \cdot 10^6$ at single photon level. This is comparable to the highest Q_i reported in literature so far.

Contents

Finis coronat opus

Chapter 1

Introduction

Ever since the introduction of the personal computer mid 20th century, mankind has found increasingly more applications that use a form of computing. Many of these applications followed because of the miniaturisation of computers, and in particular, computer processors. However, this miniaturisation has a limit due to the physical limit of how small the transistors (bits) could be. Therefore, a different way of computing has been proposed that, in theory, increases the processing power greatly. This is called *quantum computing*. As normal computing needs bits, quantum computing employs the use of *quantum bits* to represent (quantum) information. Quantum bits have constant interaction with their environment, an interaction that leads to loss of the quantum information called *decoherence*.

At the Delft University of Technology, the Quantum Transport Group (part of Kavli Institute of Nanoscience Delft) investigates the practical implementation of quantum phenomena. As part of the Quantum Transport Group, the DiCarlo Lab develops superconducting quantum circuits with applications in quantum computing, one of which is the development of transmon qubits[1]. Particularly, research is focussed on the increasing of the coherence time of the transmon qubit.

The 2D circuit quantum electronic devices (QED) processor that employs multi-transmon qubits, make use of coplanar waveguides (CPWs) for driving the qubits and for qubit cou-

pled resonators[2]. The fabrication process, the geometries and materials used to fabricate the CPW resonators and transmon qubit is similar. However, due to shorter fabrication time and straightforward measurement scheme of the latter, finding a way to increase the internal quality factor Q_i in a CPW resonator is a quick way to gain insight into methods to increase the coherence time of a transmon qubit. Lower energy loss in such a resonator is quantified by a higher internal quality factor Q_i. So far, a typical superconducting CPW resonator (using Al or NbTiN, on either Si or Al_2O_3) fabricated with standard processes, is expected to exhibit Q_is in the range of a few hundreds of thousands[3]. The current state of the art, before the present work, is represented by the work of the Martinis group (UCSB) that recently was able to produce CPW resonators with a Q_i in excess of one million ($1.7{\cdot}10^6$) at single-photon energies[4].

Previous research suggests two-level tunneling states (TLS) in dielectrics to be the main source of energy loss[5][6][7][8][9]. The location of the TLS is found to be at metal-substrate and substrate-air interfaces[10]. In this thesis, two ways of treating the metal-substrate interface are investigated, using hydrofluoric acid (HF) and *bis(trimethylsilyl)amine* (HDMS), in order to determine if different substrate treatments may lead to reduced losses. To improve the substrate-air interface, two etching techniques are compared, Reactive Ion Etching (RIE) and Deep Reactive Ion Etching (DRIE), to test the hypothesis that creating deep CPW trenches will displace the lossy interfaces away from the CPW gap region.

The main goal of this research is to characterize the Q_i at cryogenic temperature and single-photon level of superconducting CPW resonators that are fabricated using the surface preparation and etching techniques described above.

Chapter 2

Theory

2.1 Superconducting CPW quarter-wavelength resonator

In this section the transmission lineshape of an (a)symmetrical quarter-wave CPW resonator is derived. This formula will be used to fit experimental data. The microwave resonator has a length of $\lambda/4$ and one end is shorted to ground, the other capacitively coupled to a transmission feedline, as shown in Fig. 2.1. The transmission is measured as $S_{21} \equiv V_{\text{out}}/V_{\text{in}}$.

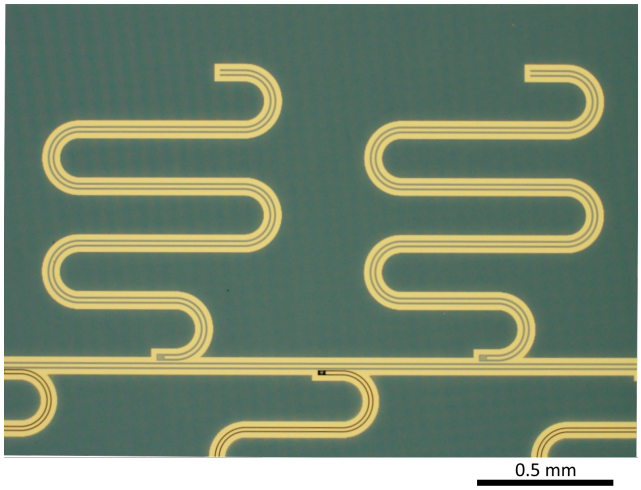

Figure 2.1: Optical image of the resonators capacitively coupled to the transmission feedline. The resonator is sometimes referred to as 'hanger' because of its characteristic form in combination with the feedline. The upper resonators and the feedline are etched using RIE, the lower resonators by using DRIE (see Chapter 3.1).

The transmission line has an impedance which, in the most ideal case, is the same left and right of the coupling point of the resonator. This is not always the case, so it is assumed that there is some impedance mismatch in the transmission line, which is taken into account in the data fitting. A schematic of the resonator circuit is shown in Fig. 2.2.

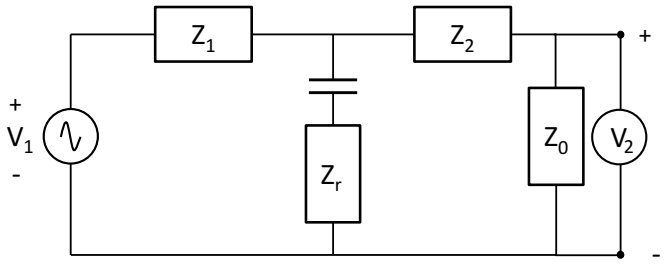

Figure 2.2: Circuit diagram model with mismatched complex impedance Z_1 and Z_2, that differ slightly from the nominal impedance $Z_0 = 50\ \Omega$. Voltages of the transmission line at the input and output are V_1 and V_2. The resonator has an impedance Z_r and coupling capacitance C to the feedline. Schematic taken from [4].

2.1.1 Quality factor

The rate at which any resonator loses its energy can be described by its quality factor Q, where a higher Q indicates a lower rate of energy loss relative to the stored energy in the resonator. Energy losses of a CPW resonator can be contributed to *internal* losses (e.g. dielectric losses) and *external* losses consisting of energy leaking through the *capacitative coupling* to the transmission line. The corresponding Qs are the internal quality factor Q_i and coupling quality factor Q_c, respectively.

The *loaded* quality factor of the resonator, Q_l, is

$$\frac{1}{Q_l} = \frac{1}{Q_i} + \frac{1}{Q_c}. \tag{2.1}$$

2.1.2 Hanger function

The transmission of a frequency through a resonator system described by

$$S_{21}^{*} = A\left(1 - \frac{\frac{Q_l}{|Q_e|}e^{i\theta}}{1 + 2iQ_l\frac{\omega-\omega_0}{\omega_0}}\right), \tag{2.2}$$

with ω the input frequency, ω_0 the resonance frequency of the resonator and A the diameter of the resonance circle, as shown in Fig. 2.4, which is equal to the width of the 3dB-point in the |S21| plot as shown in Fig. 2.3. CPW resonators with an impedance mismatch, as described in this thesis, have a characteristic asymmetrical transmission line shape. The asymmetry of the hanger is quantified by θ, the rotation angle of the resonance circle around the off-resonance point. Also an external quality factor has been introduced, Q_{e}, that is described by the following equation:

$$Q_c = \frac{Q_e}{\cos\theta} \tag{2.3}$$

Equation 2.2 does not take into account the propagation phase difference ϕ_v due to the microwave travelling to and from the resonator in the feedline, which results in moving on the edge of a circle around the origin in the real-complex plane of Fig. 2.4. Also, the transmission of the feedline is not constant with changing frequency ω, which can be taken into account using a first order approximation. Taking these conditions and plugging them into Equation 2.2 results in

$$S_{21} = A\left(1 + d\omega\frac{\omega-\omega_0}{\omega_0}\right)\left(1 - \frac{\frac{Q_l}{|Q_e|}e^{i\theta}}{1 + 2iQ_l\frac{\omega-\omega_0}{\omega_0}}\right)e^{i(\phi_v(\omega-\omega[0])+\phi_0)}, \tag{2.4}$$

where the $\omega - \omega[0]$ term is there to uncorrelate the first guess of ϕ_{v} and ϕ_0 in the fit that will be performed on the experimental data points using this function. Equation 2.4 is considered to be *the* hanger function.

Measurement data is fitted to equation 2.4 using a least squares fit where the resulting error is the residual. From this fit Q_e, Q_l and θ can be extracted, which are used to calculate Q_i from the combination of Equation 2.1 and 2.3:

$$Q_i = \frac{1}{\left(\frac{1}{Q_l} - \frac{1}{Q_e \cos\theta}\right)}. \tag{2.5}$$

The relation between Q_i and the dielectric loss term $\tan\delta_i$ is given in the equation below. This shows that a higher Q_i is the result of a lower $\tan\delta_i$. The search for high Q_i is therefore in line with the goal of this research of reducing intrinsic energy losses.

$$Q_i = \frac{1}{\tan\delta_i} \tag{2.6}$$

2.2 Photon number

In this research the Q_i of resonators at single-photon level needs to be measured. The amount of photons in the resonator, $\langle n_{photon}\rangle$, can not be measured directly. In the experiment we can only change the input power $\mathrm{P_{in}}$ of the transmission line, therefore, it is needed to relate $\mathrm{P_{in}}$ to the internal power of the resonator, $\mathrm{P_{int}}$, which has a known relation to $\langle n_{photon}\rangle$. The equations of $\mathrm{P_{int}}$ and $\langle n_{photon}\rangle$ are given by [11]

$$P_{int} = \frac{2}{\pi}\frac{Q_l^2}{Q_c}P_{in}, \tag{2.7}$$

$$\langle n_{photon}\rangle = \frac{\pi P_{int}}{\hbar\omega^2}. \tag{2.8}$$

These two equations combined gives the desired relation of $\langle n_{photon}\rangle$ and $\mathrm{P_{in}}$:

$$\langle n_{photon}\rangle = \frac{4}{\hbar\omega^2}\frac{Q_l^2}{Q_c}P_{in}. \tag{2.9}$$

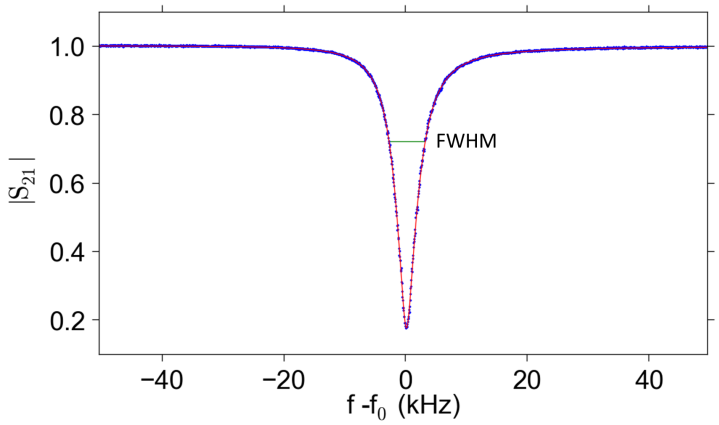

Figure 2.3: Fit of |S21| (red) using equation 2.4 to the measured transmission of a resonator resonator (blue) around the resonance peak f_0 for an input power of -95 dBm, normalized to full transmission. The green line denotes the FWHM. Asymmetry is best seen in the parametric plot of the same resonator in Fig. 2.4.

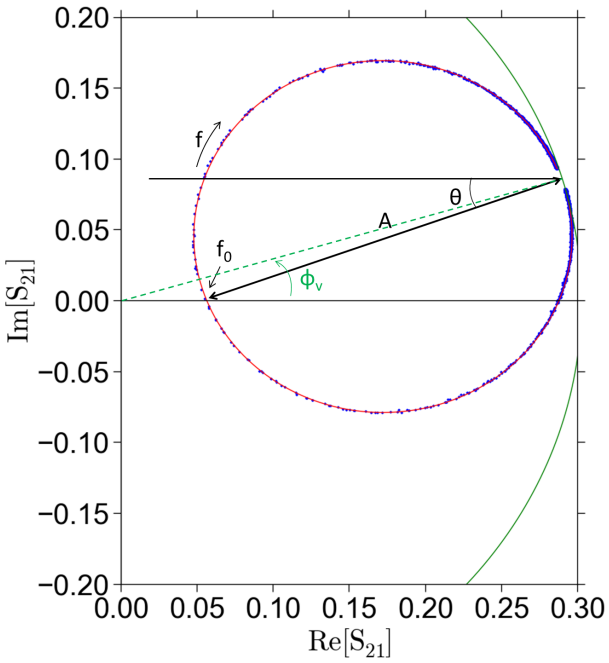

Figure 2.4: Parametric plot (blue) and fit (red) of $\mathrm{Im}[S_{21}]$ and $\mathrm{Re}[S_{21}]$ using equation 2.4 of the same data as Fig. 2.3. Precession around of the resonance circle due to ϕ_v is denoted by the green circle. Asymmetry due to impedance mismatch is quantified by θ.

Chapter 3

Experimental techniques

This chapter explains all the relevant experimental techniques. Firstly the fabrication of the CPW resonators is explained, both for standard hydrofluoric acid (HF) surface treatment as for the newly proposed HDMS treatment. Further in the fabrication section the etching of the resonators is discussed for both the standard RIE as for the newly used DRIE method. The measurement setup is described in the subsequent section, including a detailed description of the fridges and microwave setup used.

3.1 Fabrication

Planar waveguides are realized by etching a superconducting layer deposited on a substrate. For these CPW resonators, NbTiN is the chosen superconductor, deposited on top of a monocrystalline silicon substrate. The Si substrate however has come in contact with air and consequently SiO_x has formed on top of it. Most of all, the formation of oxides needs to be prevented because of their high density of defects (TLS), which are responsible for energy losses at single-photon energies [9]. Before the sputter deposition of the NbTiN, two surface preparation methods have been used on the silicon substrate, namely HF and HDMS. Every fabricated **device set** has a **sample** treated with *only* HF and a **sample** treated with HF *and* HDMS.

3.1.1 Silicon surface treatment

The surface of a Si wafer, without any intentional processing, is covered with native oxides, as shown in Fig. 3.1.

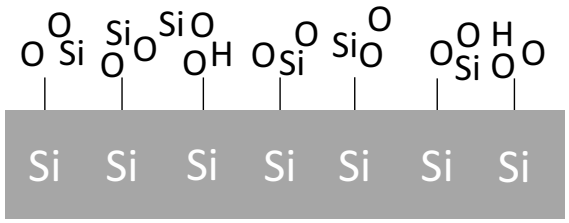

Figure 3.1: Simplified view of the Si substrate surface before any treatment

The amorphous native oxide layer is ∼1 nm thick and has a high density of microscopic defects, dangling bonds and charge traps, generally referred to as TLS. In order to achieve an interface with a low amount of defects between the superconductor and the substrate, before any deposition of NbTiN can be done, these oxides need to be removed using HF.

3.1.1.1 HF surface treatment

Dipping the Si substrate in HF results in the surface being terminated with hydrogen atoms, as shown in Fig. 3.2. This is done for both **samples** of every **device set**.

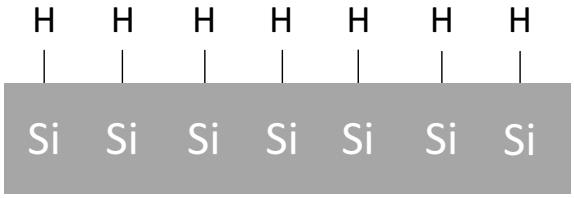

Figure 3.2: Simplified view of the Si substrate without the native oxides after treatment with HF. Hydrogen has bonded to the surface of the Si.

3.1.1.2 HDMS surface treatment

HDMS is short for *bis(trimethylsilyl)amine*, or in molecular formula: $[(CH_3)_3\,Si]_2\,NH$. This liquid is widely used in the organic chemistry and in microelectronic processing as an adhesion layer. After the oxide cleaning with HF, one of the two samples for each set has been treated with HDMS to create the surface as shown in Fig. 3.3

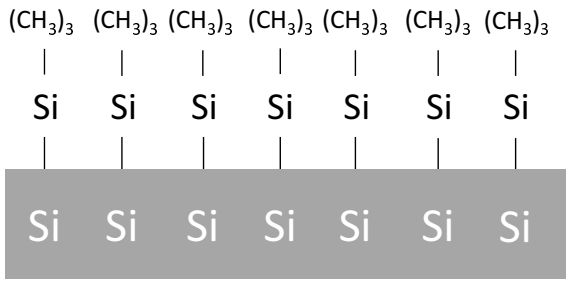

Figure 3.3: Simplified view of the Si substrate with native oxides removed after treatment with HF and HDMS. $Si\,(CH_3)_3$ has bonded to a Si atom of the substrate.

3.1.2 Reactive Ion Etching (RIE)

In this section the process of Reactive Ion Etching (RIE) and its application is explained. A RIE system consists of a vacuum chamber with sample holder that is placed between two electrodes, as shown in Fig. 3.4. A plasma of SF_6^+ and He is created in the vacuum chamber and is accelerated towards the surface of the sample. The reactive gas molecules collide with the substrate effectively etching its surface, by means of both chemical and physical processes.

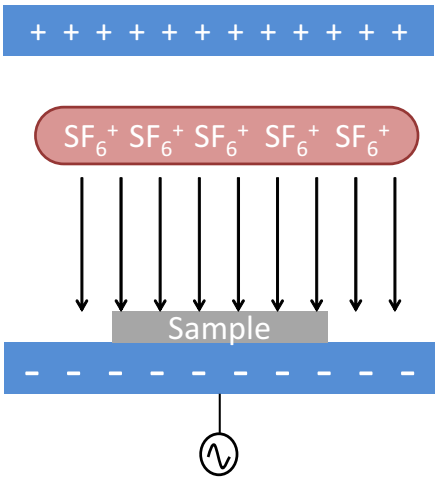

Figure 3.4: Schematic representation of the RIE process. A plasma of SF_6^+ and He bombards the a sample due to acceleration by the electrodes, effectively etching the sample.

3.1.3 Deep Reactive Ion Etching (DRIE)

In this section the process of Deep Reactive Ion Etching (DRIE) and its application is explained. A DRIE system is in essence the same as RIE system (Fig. 3.4), with the distinction that now the gases present in the chamber are alternated. The plasma of SF_6^+ and He is repeatedly alternated with a plasma of C_4F_8, that results in the deposit of a chemically-inert passivation layer, PTFE. Each phase lasts for 7 and 2.5 seconds, respectively. The PTFE protects the entire substrate, including the etched trench and its sidewalls. However, the SF_6^+ is accelerated directionally, colliding with the bottom of the trench and less energetically with the sidewalls. The relatively thin PTFE layer on the bottom of the trench is then

etched away faster than the sidewalls, leaving the sample substrate open at the bottom for further etching. This DRIE procedure allows for selective deep etching, which is not possible using RIE. This process is schematically shown in Fig. 3.6. The DRIE and RIE process can both be tweaked in a certain way to perform not only downward etch (anisotropic), but also sideways (isotropic), effectively underetching the NbTiN layer, creating free standing metal edges as can be seen in Fig. 3.5(b).

A final (optional) step after etching using the DRIE method is a passivation layer of PTFE that can be deposited on only the Si sidewalls, potentially protecting them from oxidation in air. SEM pictures of CPWs etched using different DRIE procedures are shown in Fig. 3.5.

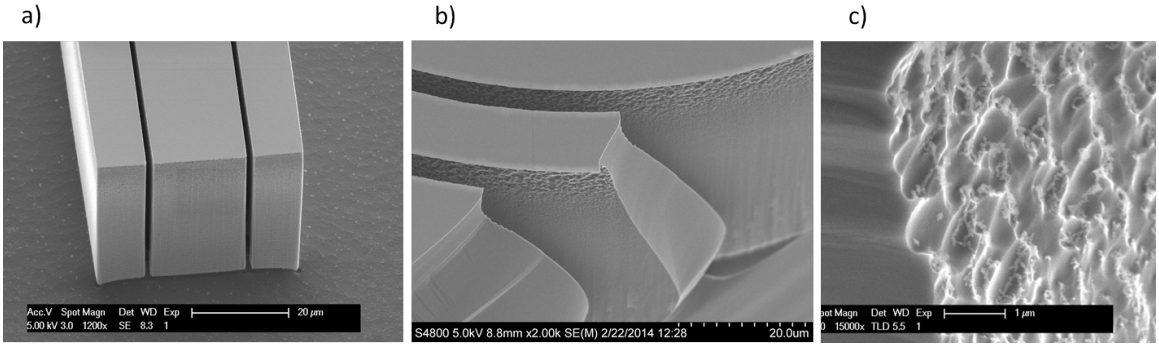

Figure 3.5: a) CPW etched using only anisotropic DRIE recipe. b) CPW etched using anisotropic followed by isotropic DRIE recipe. Underetch of $\sim$2 µm is visible. c) Detail of sidewall after PTFE passivation.

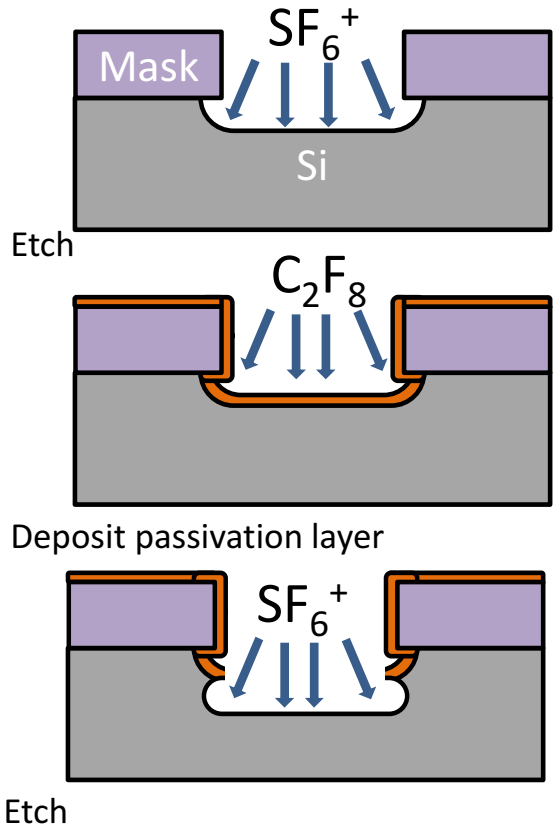

Figure 3.6: Schematic representation of the DRIE process. A plasma of SF_6^+ bombards the a sample due to acceleration by remote electrodes, effectively etching the sample. Subsequently a C_4F_8 plasma is pumped in, forming a PTFE layer everywhere on the surface. Directional etching is achieved by faster removal of the PTFE on the bottom of the etched trench than removal of the sidewall PTFE, effectively etching only downwards.

3.1.4 Resonator fabrication

After the proper surface cleaning, a layer of 160 nm of NbTiN is deposited on top of the Si substrate. The NbTiN has a typical T_c of 15.5 K and resistivity of 100 µΩ cm. Subsequently, a layer of SAL601 is spun and a first e-beam lithography is used to pattern the CPW structures. The *feedline* and *half* of the resonators will be etched using the RIE method, having CPW gaps 5 µm wide and 100 nm deep into the Si substrate. After the RIE resonators are etched and the sample has been cleaned, a 6 µm resist is applied which serves as etching mask. E-beam lithography is used to pattern the resonators that will

subsequently be etched using the DRIE method. DRIE resonators have CPW gaps of 2 µm, but are significantly deeper, up to 80 µm. This process is schematically shown in Fig. 3.7. All CPW structures used in this thesis have a center conductor of 12 µm wide, resulting in ∼50 Ω impedance for RIE and ∼70 Ω for DRIE resonators. The difference is due to an effective ϵ_r of the trenched substrate of about 3.9 instead of 11.9 for bare Si. The thicker resist is necessary so the NbTiN will not be etched during the DRIE process. An example of overetching is shown in Fig. 3.8.

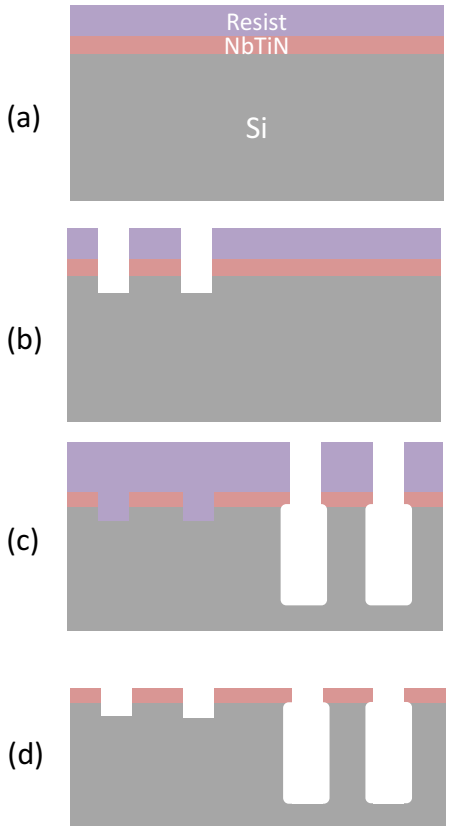

Figure 3.7: Schematic representation the resonator etching process. (a) Silicon substrate coated with NbTiN and etching mask. (b) E-beam litography, develop and RIE etch. (c) 6 µm thick resist is applied, followed by e-beam lithography, develop and DRIE process. (d) Cleaning the sample leaves only the etched trenches in the Si and NbTiN on top.

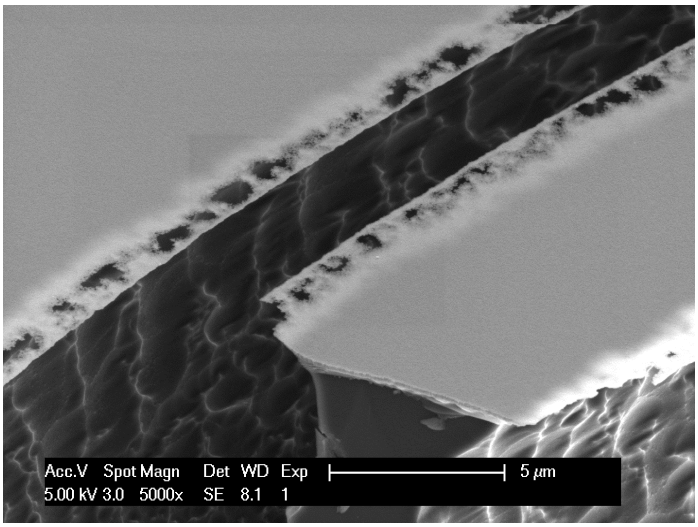

Figure 3.8: SEM picture of an excessively etched NbTiN toplayer, which results in mousebites on the NbTiN part that hangs above the underetched Si. Notice the sidewall roughness in comparison to Fig. 3.7 as result of the underetch.

After all etching steps have been done, a resulting sample is as shown in Fig. 3.9. The lumped elements and transmon qubits that are also present on the sample are there to test the new fabrication techniques for these types of structures. In this thesis these will not be discussed further.

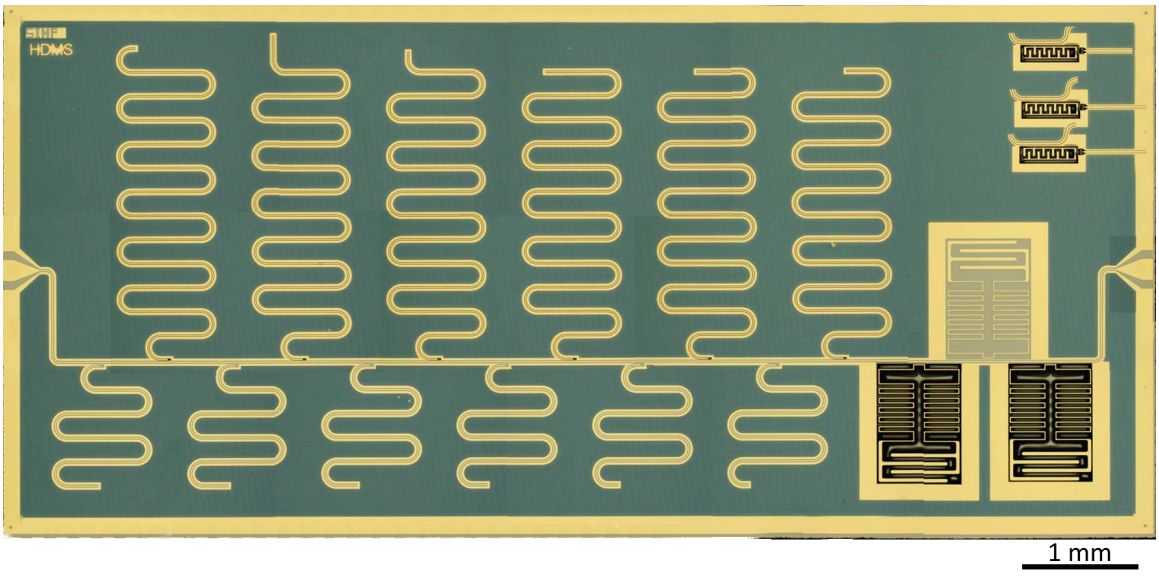

Figure 3.9: Optical microscope picture of a HDMS treated sample. The resonators on the top part of the sample are etched using DRIE, the bottom and feedline with RIE. Note that the layout of every sample is independent of its surface treatment (HF/HDMS).

3.1.5 Sample inspection

For every device set there are resonators that do not appear in the measurements or at the expected frequency, accordingly they are called 'broken'. A resonator can be broken in different ways, e.g. a local short due to bad etching (Fig. 3.10a), resist residue in the CPW trench or rough edges of the NbTiN (Fig. 3.10b). The reason for such defects can happen at several of the fabrication steps, and is likely to happen less frequently as the fabrication recipe gets more optimized.

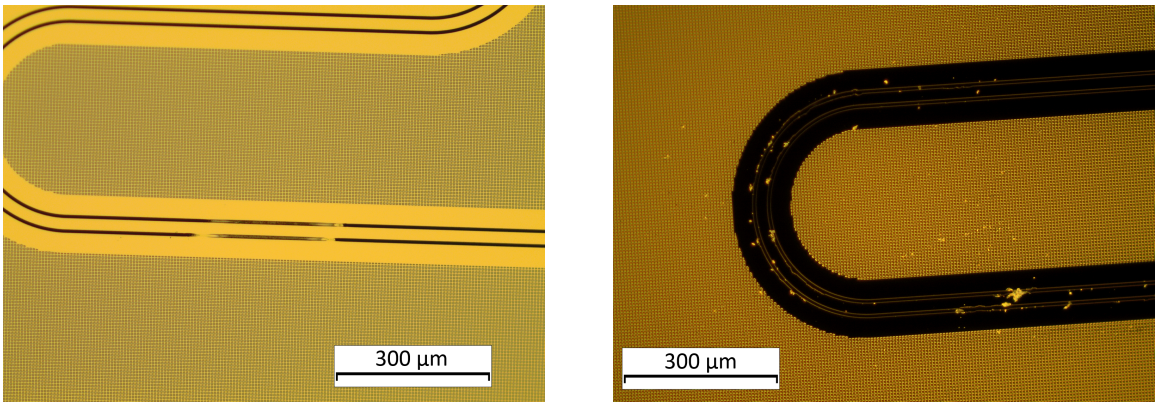

(a) (b)

Figure 3.10: (a) Resonator that locally has no etch due to a resist defect, shorting it. The resonator will resonate at higher frequency than the expected value. (b) Resonator that locally has resist stuck in the CPW trench and rough edges, due to the application of ultrasound in the final cleaning step.

3.2 Measurement setup

The two samples, HF and HDMS, of each device set are glued in their own copper printed circuit board (PCB) and bonded by Al wires, see Fig. 3.11.

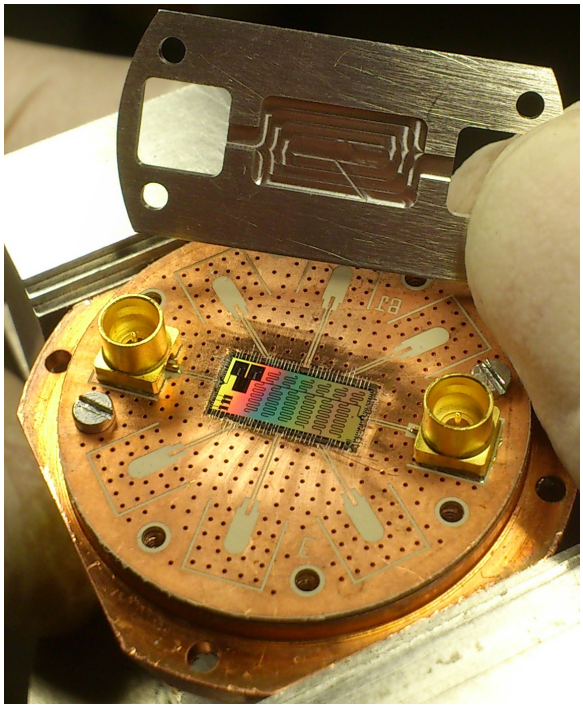

Figure 3.11: A sample mounted on the copper PCB with the transmission feedline connected to the two SMP connectors.

The transmission feedline of the sample is connected to two SMP connectors on each side. Aluminium wirebonding has been used to connect the feedline to the ground and to ensure mechanical stability and thermalization of the sample. For increased magnetic shielding, an aluminium shim is placed on top of the sample, completely covering albeit not touching it. The fully assembled PCB is screwed onto an Octobox sample holder.

For the S_{21} measurement of NbTiN CPW resonators, superconductivity of the NbTiN and suppression of thermal noise are necessary, which are achieved by placing the samples in fridges with a $T_{base} < 1K$. The microwave input signal and readout have been done with a vector network analyzer (VNA, Rohde&Schwarz ZVM 10 MHz-20 GHz). To suppress thermal noise and to reach single-photon energy level, heavy signal filtering is needed. At

the same time, amplification of the readout signal is necessary for a meaningful readout. A schematic of the measurement setup is shown in Fig. 3.13. As shown in the figure, resonator samples have been characterized in two fridges, namely LaFerrari and LaVespa. Further specifications of the fridges is given in the next two sections.

3.2.1 Fridges

3.2.1.1 LaFerrari

Most measurements have been performed in the LaFerrari fridge, a cryogen free ^{3}He/^{4}He dilution fridge manufactured by Leiden Cryogenics, that has a base temperature of ∼20 mK. The sample, connected to the PCB, was placed on a copper sampleholder inside an aluminium ball (from Ikea) coated with SiC and stycast. This ball was placed, in a concentric fashion, inside *another* aluminium ball with the same coating in order to improve the shielding of the sample from as much external magnetic flux and IR radiation as possible. The microwave input and output cables are equipped at the feed through of the aluminium balls with in-line home built eccosorb IR filters. The inside of the balls with connected sample is shown in Fig. 3.12a. The two-ball device with the sample was thermally anchored on the fridge mixing stage, as shown in Fig. 3.12b.

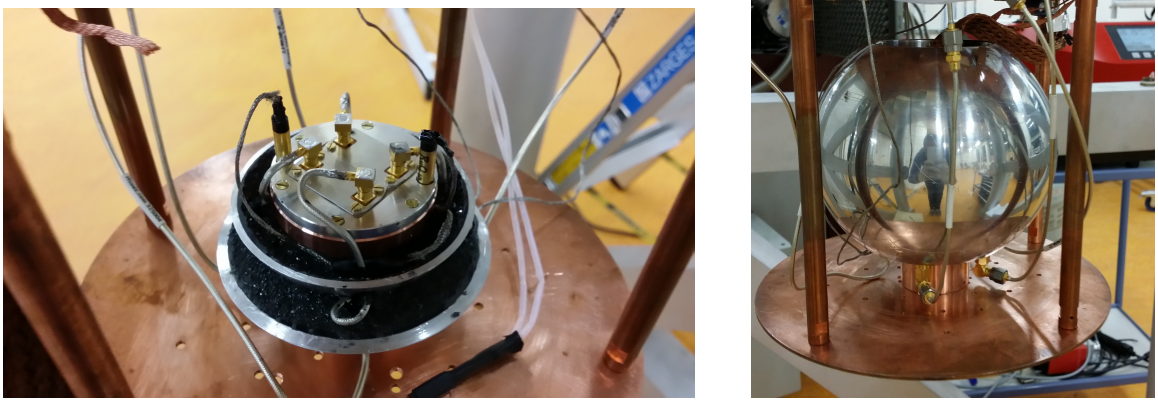

(a) (b)

Figure 3.12: (a) Picture of the inside of the aluminium balls. There are two microwave cables going in and two cables going out. (b) The aluminium balls as mounted on a stage achored to LaFerrari's mixing plate.

3.2.1.2 LaVespa

Because of its short cooldown time (∼2 hours), the LaVespa fridge has been used for quick sample characterization. LaVespa is a Heliox ^{3}He cryostat from Oxford Instruments consisting of three stages. The inner vacuum chamber (IVC) is placed inside a ^{4}He dewar (stage 1). The IVC has a pot (1K-pot) which lets Helium in from the dewar through a needle valve and is being pumped by a ^{4}He pump. Under low pressure this pot can reach temperatures as low as ∼1.6 K (stage 2). The coldest stage is a ^{3}He pot, that can be pumped on using a internal pump (SORB). For SORB temperatures below ∼10 K, it effectively pumps on the ^{3}He condensed liquid reservoir in the pot, cooling it down to T_{base}∼250 mK. Cooldown of this fridge takes ∼2 hours and has a holdtime of ∼48 hours, until the ^{3}He pot is empty. After that, recondensing of the ^{3}He to the 1K-pot is needed. This is done by heating up the SORB to ∼25 K, releasing the ^{3}He in about 30 minutes. Magnetic shielding is achieved in LaVespa by two concentric cylinders encapsulating the IVC, made of lead and a Mu-metal. IR shielding is realized by the same home made eccosorb filters as described for LaFerrari.

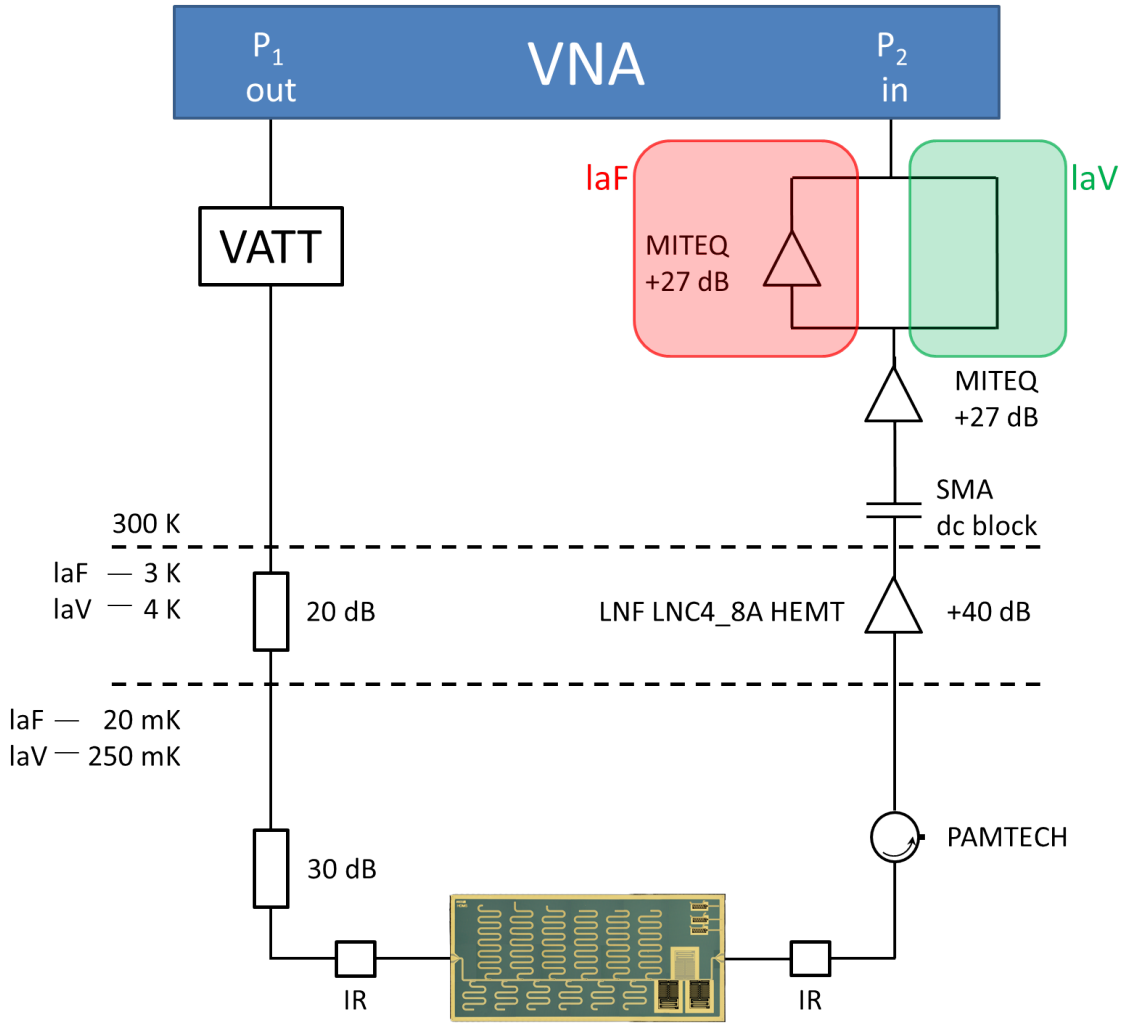

Figure 3.13: Device in the experimental setup. The sample is cooled either in the LaFerrari (laF) fridge (∼20 mK) or in the LaVespa (laV) fridge (∼250 mK). A microwave signal is generated and measured by a VNA, going from port 1 to port 2. At room temperature the output signal of the VNA is attenuated by a variable attenuator (VATT) which can attenuate in steps of 2dB from 0 to 100dB. At 4 or 3K for LaVespa and LaFerrari, respectively, there is a 20 dB attenuator. At T_{base} there is a 30 dB attenuator, with two homemade eccosorb filters at in- and output of the sample. Following the eccosorb filter at the output is a PAMTECH circulator. At the 4 or 3K stage the signal is amplified with 40 dB. In LaFerrari, this amplifier has a noise temperature of ∼2.5K, while in LaVespa this is ∼80K. At room temperature there is a SMA dc block, followed by a MITEQ amplifier of +27 dB. In LaFerrari there is a second MITEQ +27 dB amplifier, in LaVespa there is not.

Chapter 4

Results

4.1 Description of measured devices

4.1.1 Set 1

Device set 1 consists of two separate samples treated with HF or HDMS. Of each of the two differently treated samples, 6 resonators are created using DRIE and 6 by using RIE, all *without* surface PTFE passivation. The resonance frequency of each resonator is shown in Table 4.1. Resonators that are not present in the table are broken. Q_i measurements on this device have been performed in LaVespa first, then after approximately one month of air contact, Q_i has been remeasured in LaFerrari. In this fridge the measurement of Q_i as a function of temperature has also been performed. Lastly, the device was returned to LaVespa. Q_is are calculated using a fit to $|\mathrm{S}_{21}|$ in the first two fridges and in the last by fitting to the complex S_{21}. The Q_i of all further sets is determined using the complex S_{21} fit.

Table 4.1: Resonator type, label and f_0 for every resonator on device set 1 of samples treated with (a) HF and (b) HDMS.

(a)

HF		
Type	Label	f_0 (GHz)
DRIE	13	4.017
	14	4.097
	15	4.179
	16	4.257
	17	4.308
RIE	0	5.667
	1	6.921
	2	7.003
	3	7.083
	4	7.164
	5	7.246

(b)

HDMS		
Type	Label	f_0 (GHz)
DRIE	0	4.122
	1	4.128
	2	4.194
	3	4.299
	4	4.354
	5	4.397
RIE	8	6.927
	9	7.007
	10	7.081
	11	7.160
	12	7.238
	13	7.316

4.1.2 Set 2

Device set 2 is designed and produced to be the same as set 1, to see if the results from this set can be reproduced. In order to confirm the matching of resonance frequency to the etching method used (DRIE/RIE), one alteration had been made to set 2. One resonator of DRIE has purposefully been shifted to ∼6.5 GHz. All resonance frequencies can be found in Table 4.2. Resonators that are not present in the table are broken. Q_i measurements on this device have been performed in LaFerrari at base temperature.

Table 4.2: Resonator type, label and f_0 for every resonator on device set 2 of samples treated with (a) HF and (b) HDMS. Note the frequency shifted DRIE resonator in bold, which is broken for the HDMS sample.

(a)

HF		
Type	Label	f_0 (GHz)
DRIE	1	4.144
	2	4.201
	3	**6.542**
	4	4.432
	5	4.381
	6	4.423
RIE	10	7.040
	11	7.115
	12	7.192
	13	7.268
	14	7.345

(b)

HDMS		
Type	Label	f_0 (GHz)
DRIE	1	4.16
	2	4.217
	4	4.336
	5	4.385
	6	4.443
RIE	8	6.927
	9	7.007
	10	7.081
	11	7.160
	12	7.238
	13	7.316

4.1.3 Set 3

The last set that has been measured is designed to be the same as set 2, but now the final PTFE surface passivation has been applied to measure a possible improvement in ageing stability, as is explained in Chapter 3.1. All resonance frequencies can be found in Table 4.3. Resonators that are not present in the table are broken. Q_i measurements on this device have been performed in LaFerrari first and subsequently directly in LaVespa. The sample has been kept in vacuum as much as possible after fabrication and between cooldowns. A subsequent cooldown after long exposure to air will be needed to further quantify ageing stability, but this is not performed within this present work.

Table 4.3: Resonator type, label and f_0 for every resonator on device set 3 of samples treated with (a) HF and (b) HDMS. Note the frequency shifted DRIE resonator in bold.

(a)

HF		
Type	Label	f_0 (GHz)
DRIE	1	4.242
	2	4.261
	3	**6.497**
	4	4.329
	5	4.390
	6	4.451
RIE	9	6.951
	12	7.178
	13	7.254
	14	7.330

(b)

HDMS		
Type	Label	f_0 (GHz)
DRIE	1	4.210
	2	4.283
	3	**6.693**
	4	4.428
	5	4.457
	6	4.307
RIE	9	6.956
	10	7.039
	11	7.118
	12	7.199
	13	7.281
	13	7.363

4.2 Results per device

4.2.1 Set 1: LaVespa

4.2.1.1 HDMS

Measurements of Q_i as a function of $\langle n_{photon} \rangle$ are shown in Fig. 4.1. The $\langle n_{photon} \rangle$ of the RIE resonators is ∼2 orders of magnitude lower at the same $\mathrm{P_{in}}$ as the DRIE resonators, because of a lower Q_i (see Equation 2.9). The two lowest and highest power input for resonator 1 and the lowest power of resonator 0 are not shown in this graph due to a jump in the transmission of the frequency sweep around the $\mathrm{f_0}$ resulting in an inaccurate fit.

The Q_is of DRIE resonators is generally a factor of ∼2 higher than the RIE resonators and have a maximum Q_i of $3.76{\cdot}10^6 \pm 9.4{\cdot}10^4$ at the lowest reached $\langle n_{photon} \rangle$ of that resonator, which is of the order of 10^2. The Q_i dependence of the $\langle n_{photon} \rangle$ of all the RIE resonators has a saw tooth shape which is different from the shape of the DRIE resonators Q_i.

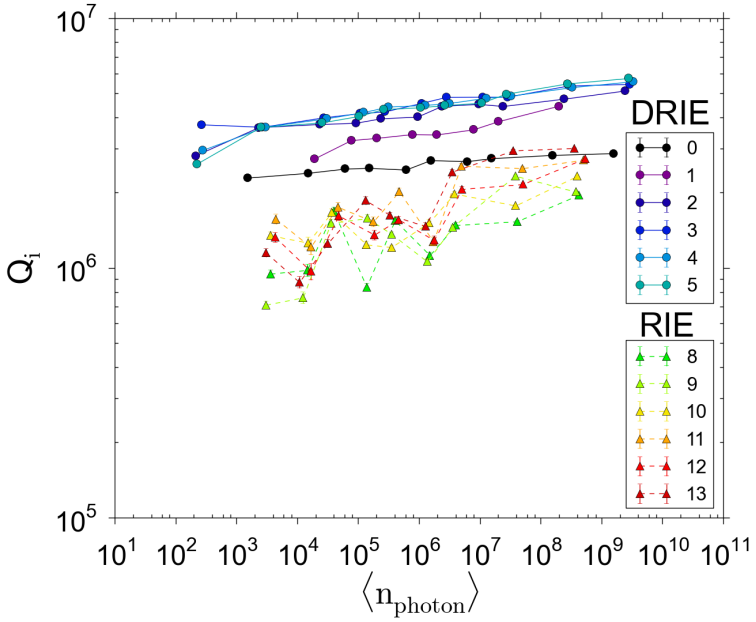

Figure 4.1: Q_i as a function of $\langle n_{photon} \rangle$ in the resonator for the HDMS sample of set 1 measured in LaVespa. Solid and dashed lines represent the DRIE and RIE method, respectively.

4.2.1.2 HF

The measurement of Q_i as a function of $\langle n_{photon} \rangle$ for the HF treated sample of set 1 is shown in Fig. 4.2. The RIE resonators all have a Q_i of the order of $\sim 10^5$ at lowest photon number, whereas DRIE resonators all have quality factors above 10^6. Power dependence of the Q_i is for all resonators shown in Fig. 4.2 is observed, but this is near to negligible (Q_i for lowest and highest power input differ a factor ~ 2).

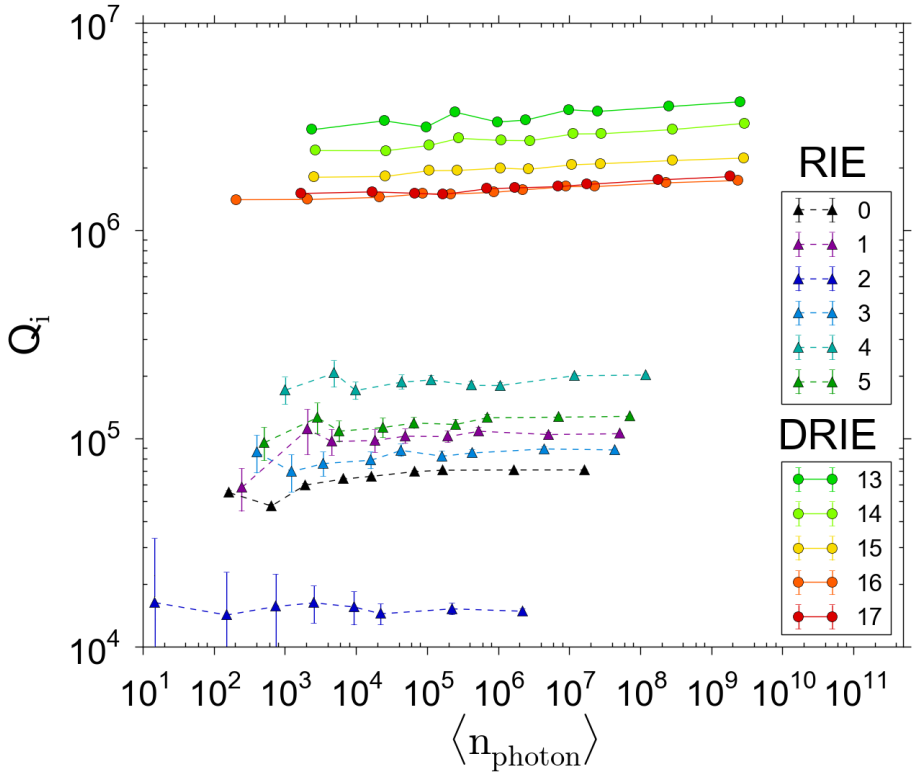

Figure 4.2: Q_i as a function of $\langle n_{photon} \rangle$ in the resonator for the HF sample of set 1 measured in LaVespa. Solid and dashed lines represent the DRIE and RIE method, respectively.

4.2.2 Set 1: LaFerrari

4.2.2.1 HDMS

Remeasuring the HDMS treated sample of set 1 in LaFerrari resulted in the graph shown in Fig. 4.3. For the first time we see RIE and DRIE resonators have Q_is in the same region, between $8{\cdot}10^5$ and $3{\cdot}10^6$ because the DRIE resonators have lower Q_i than when measured in LaVespa. RIE resonators have a stronger power dependence than the DRIE and converge to the same point of Q_i of $\sim 8{\cdot}10^5$ and $\langle n_{photon} \rangle$ of $\sim 2{\cdot}10^2$.

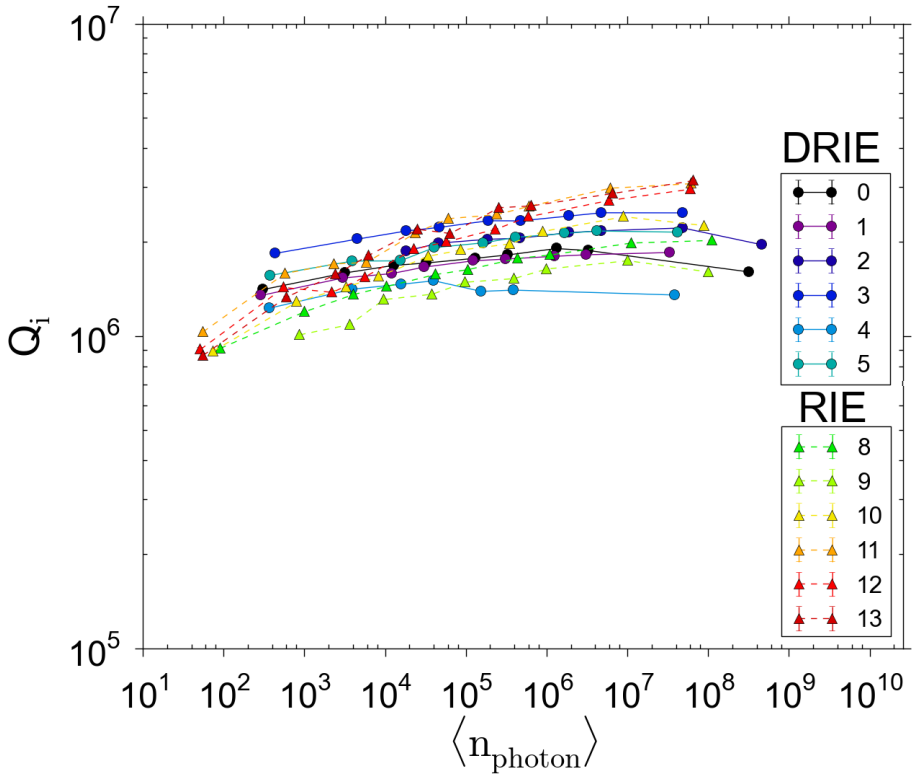

Figure 4.3: Q_i as a function of $\langle n_{photon} \rangle$ in the resonator for the HDMS sample of set 1 measured in LaFerrari. Solid and dashed lines represent the DRIE and RIE method, respectively.

4.2.2.2 HF

The measurement of the HF treated sample of set 1 in LaFerrari is shown in Fig. 4.4. All RIE resonators have lower Q_i than the DRIE resonators, except for resonator 1 which is comparable to resonator 13 of DRIE, both having a Q_i of $\sim 10^6$ at their respective lowest measured photon number.

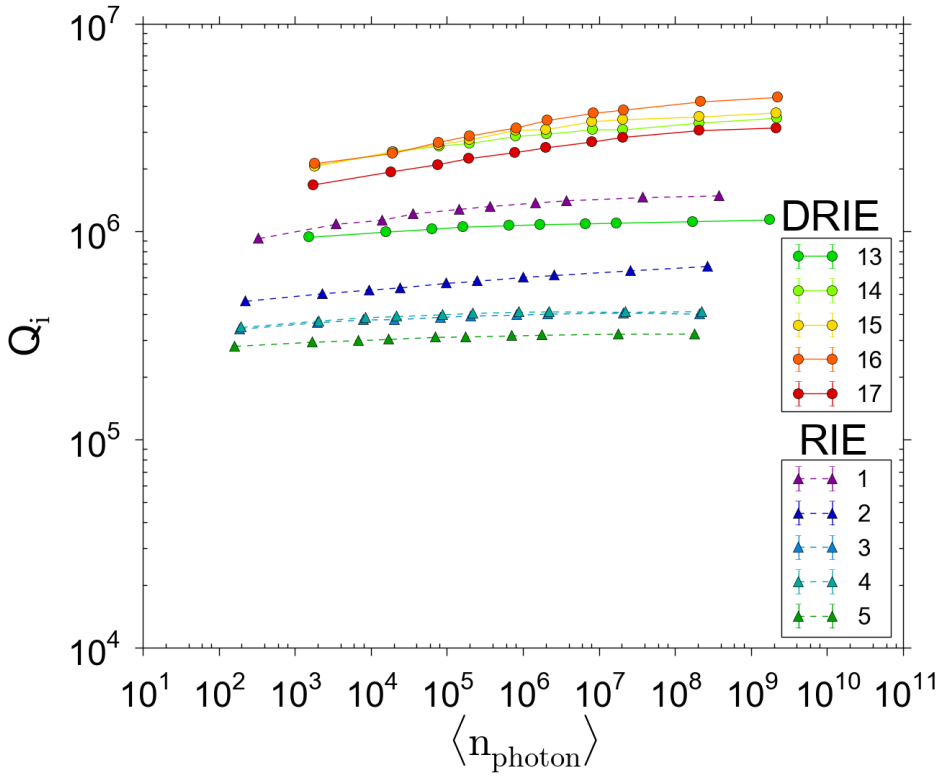

Figure 4.4: Q_i as a function of $\langle n_{photon} \rangle$ in the resonator for the HF sample of set 1 measured in LaFerrari. Solid and dashed lines represent the DRIE and RIE method, respectively.

4.2.3 Set 1: LaVespa(2)

4.2.3.1 HDMS

Measuring the first sample set in LaVespa again resulted in the graph shown in Fig. 4.5. Contrary to what has been shown in previous graphs, the DRIE resonators now all have lower Q_i than the RIE ones and do not show any power dependence. The dependence of Q_i on $\langle n_{photon} \rangle$ for resonator 12 is not like the other RIE resonators and the transmission also has a different line shape than all other resonators on this HDMS treated sample, asymmetrical instead of symmetrical. The value of Q_i for resonator 11 at lowest $\langle n_{photon} \rangle$ is higher than expected, in comparison to resonators 9 and 10 and what has been observed in the previous measurements.

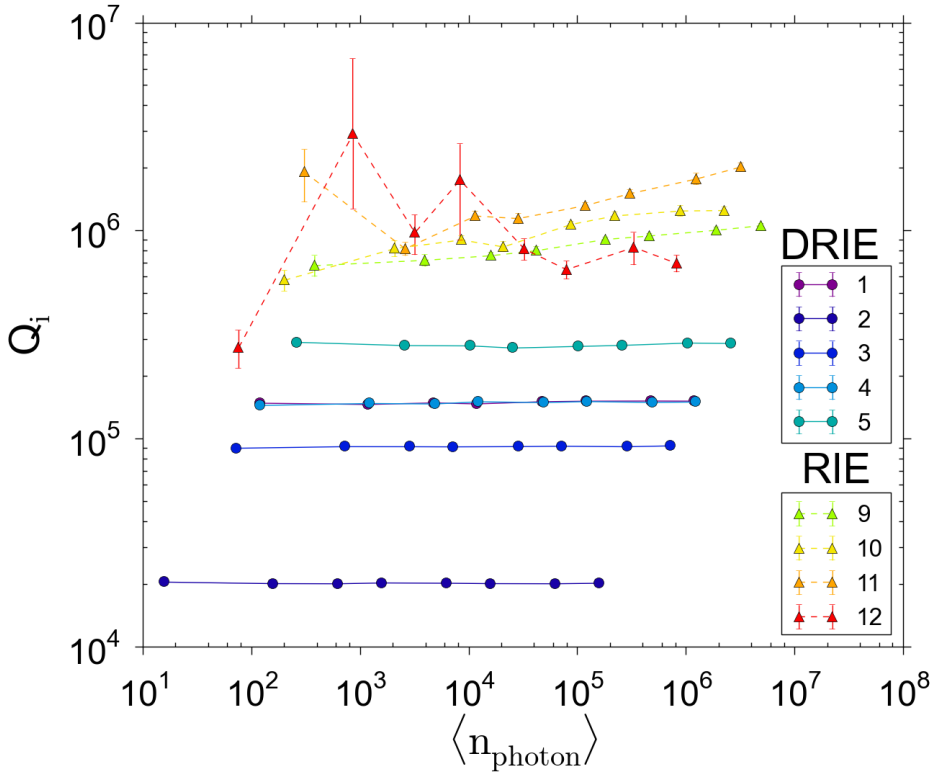

Figure 4.5: Q_i as a function of $\langle n_{photon} \rangle$ in the resonator for the HDMS sample of set 1 measured in LaVespa for the second time. Solid and dashed lines represent the DRIE and RIE method, respectively.

4.2.4 Set 1: Temperature sweep

4.2.4.1 HF

A temperature sweep has been performed for four resonators on the HF sample, of which two etched using DRIE and two using RIE. Figure 4.6 shows the heater voltage dependence of the Q_i as a function of photon number. A calibration curve of the temperature as a function of heater voltage can be found in Appendix A. Increasing the temperature saturates the TLS which results in a higher Q_i for every resonator measured. The shape of the traces differ, RIE resonator 3 performs increasingly worse for decreasing $\langle n_{photon} \rangle$ and for increasing V_H this decrease is less, from Q_i=4·10^5 to 2.8·10^5 for V_H=0.1 V and to 3.4·10^5 at V_H=0.2V at $\langle n_{photon} \rangle$ in the order of 10.

The dependence of Q_i as a function of $\langle n_{photon} \rangle$ for RIE and DRIE resonators follows different trends for changing V_H.

Both DRIE resonators have a lower $\langle n_{photon} \rangle$ dependence in Q_i at higher V_H, resulting in a difference of ∼1.1·10^6 in Q_i for $\langle n_{photon} \rangle$ around 10^2 for resonator 16 and ∼0.8·10^6 for resonator 15.

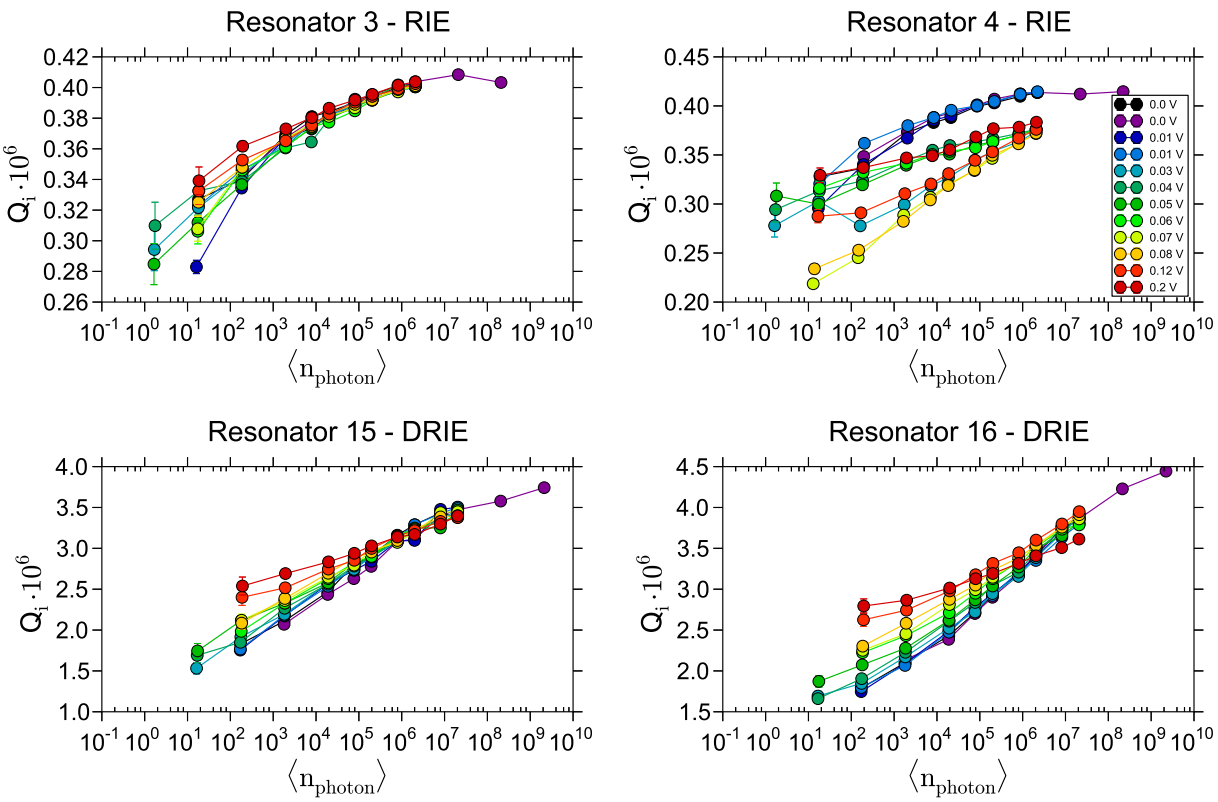

Figure 4.6: Q_i as a function of $\langle n_{photon} \rangle$ for two DRIE and two RIE resonators of the HF sample of the first device set for changing V_H.

4.2.4.2 HDMS

A temperature sweep has also been performed for four resonators on the HDMS sample, of which two etched using DRIE and two using RIE. Figure 4.7 shows the heater voltage dependence of the Q_i as a function of $\langle n_{photon} \rangle$. RIE resonators have a decrease in Q_i for highest $\mathrm{P_{in}}$($\langle n_{photon} \rangle \approx 10^6$) of about $5{\cdot}10^5$ in comparison to near-base temperatures but for any V_H the Q_i,$\langle n_{photon} \rangle$ dependence follows the same trend. DRIE resonators have a trend of less decrease in Q_i for lower $\langle n_{photon} \rangle$ when V_H is higher, for resonator 5 at V_H=0.12V and V_H=0.08V the Q_i is constant for the lowest two $\mathrm{P_{in}}$.

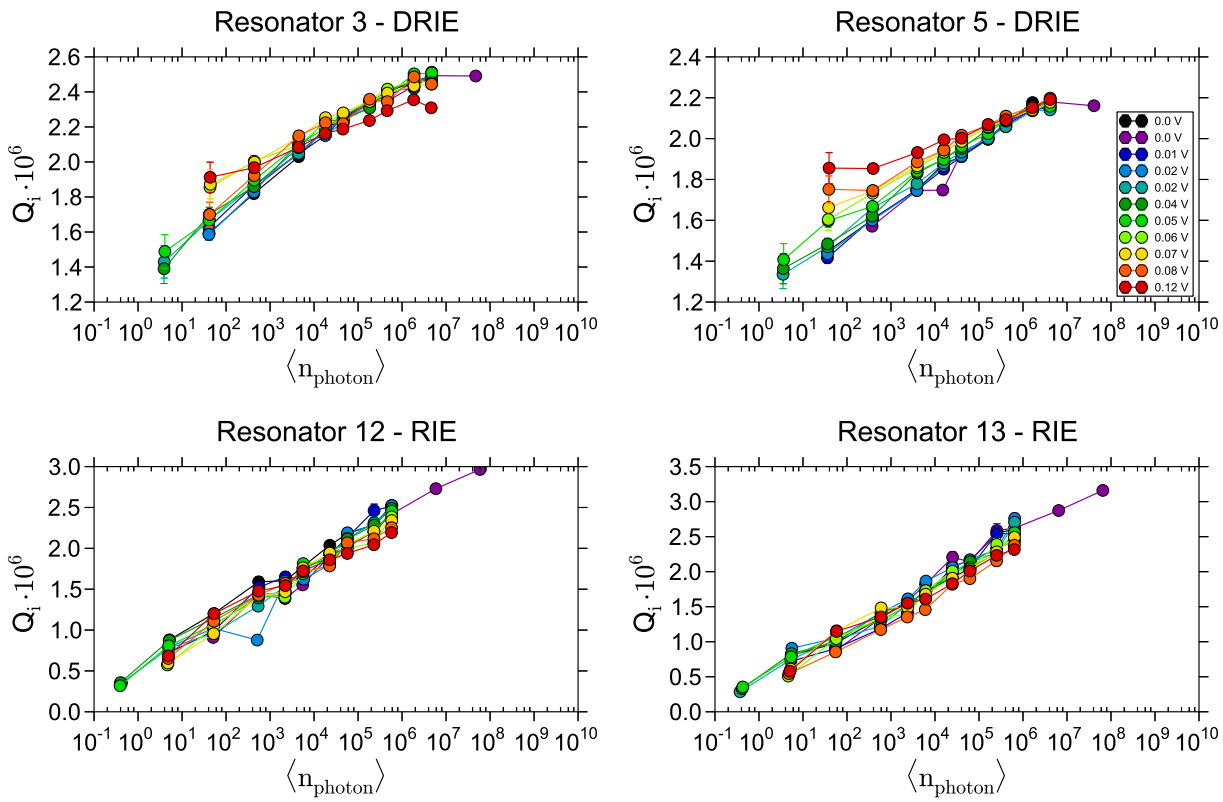

Figure 4.7: Q_i as a function of $\langle n_{photon} \rangle$ for two DRIE and two RIE resonators of the HDMS sample of the first device set for changing V_H.

4.2.4.3 HF & HDMS

A more qualitative analysis the Q_i as a function of heater voltage is shown in Fig. 4.8.

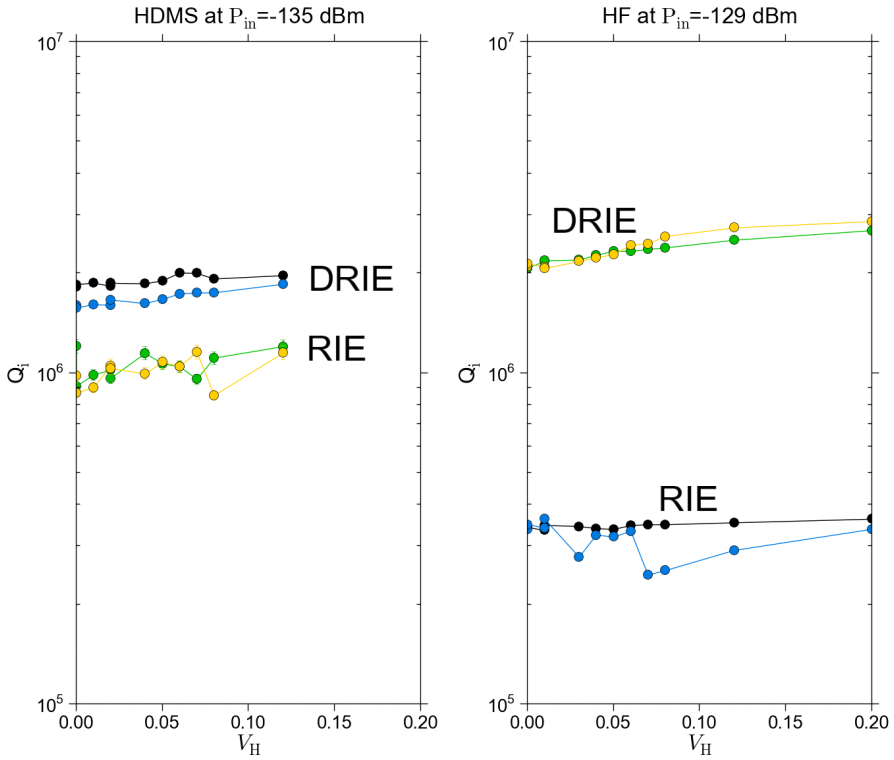

Figure 4.8: Q_i as a function of $\langle n_{photon} \rangle$ for two DRIE and two RIE resonators of the HDMS sample of the first device set for changing V_H.

4.2.5 Set 2

4.2.5.1 HF

The Q_i of the resonators of the HF treated sample of set 2 is shown as function of $\langle n_{photon} \rangle$ in Fig. 4.9.

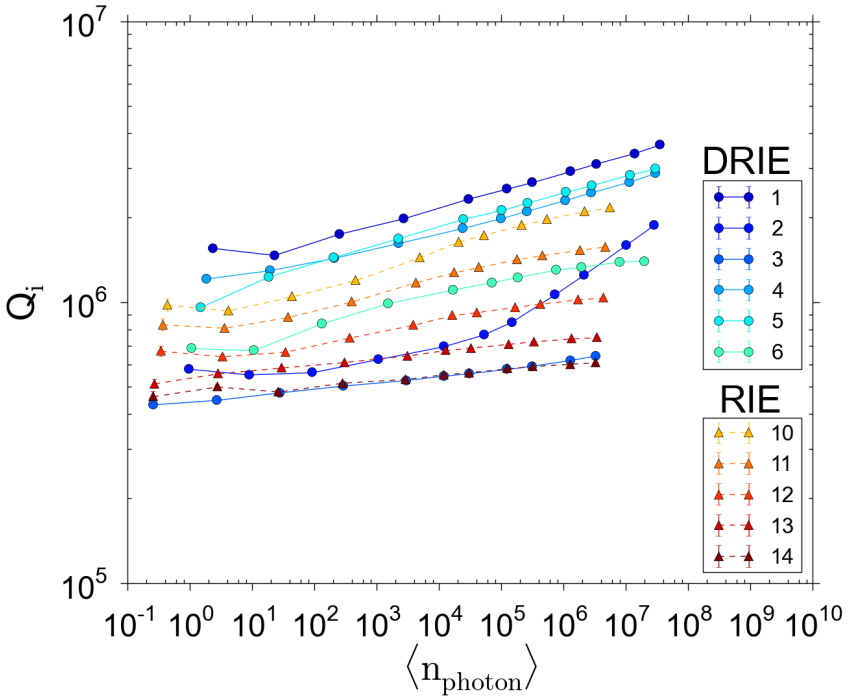

Figure 4.9: Q_i as a function of $\langle n_{photon} \rangle$ for the HF treated sample of device set 2. Solid and dashed lines represent the DRIE and RIE method, respectively.

Of the resonators made using the DRIE method, number 1, 4 and 5 are performing the best, having Q_i above one million with a maximum of $1.56 \cdot 10^6$ at the lowest power whereas the Q_is of 2, 3 and 6 are comparable to the quality factor range of the RIE resonators. At the same time the decrease in Q_i between $\langle n_{photon} \rangle = 10^4$ and 10^6 for resonator 2 is $1.31 \cdot 10^6$ in comparison to e.g. $0.89 \cdot 10^6$ for resonator 4.

4.2.5.2 HDMS

Having established a baseline using the HF samples, now is shown how the resonators on the HDMS treated samples perform for again both DRIE and RIE methods. Figure 4.10 shows the power dependence of the Q_i of the resonators for both DRIE and RIE treated sample set 2. We see that DRIE resonator 6 is comparable with respect to quality factor to the best performing RIE resonators 10 and 11, all other DRIE resonators outperform the RIE ones in Q_i, reaching a $Q_{\mathrm{i,max}}$=2.24·10^6±1.34·10^5 at single-photon level.

All RIE resonators have a trend of decreasing more in Q_i when going from single-photon to 10^{-1} photon regime of an average of Q_i=4.73·10^5. In comparison, going from $\langle n_{photon}\rangle$=$10^2$ to 10^1 has an average decrease of Q_i=1.84·10^5. This trend is not visible for the DRIE resonators, with the exception of resonator 2. The fit of the transmission of the RIE resonators is accurate and not influenced by noise, which shows in the errobars in Fig. 4.10.

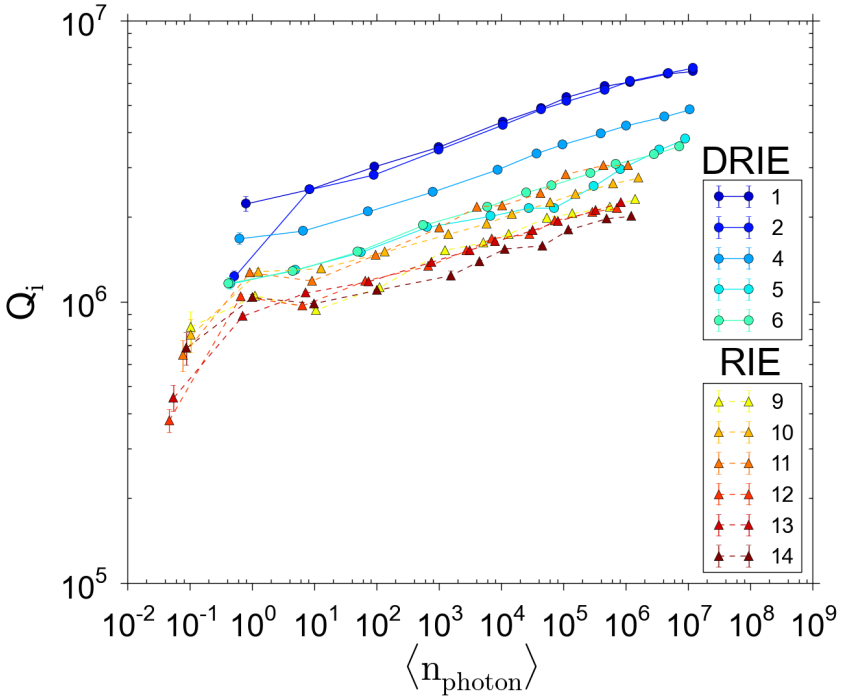

Figure 4.10: Q_i as a function of $\langle n_{photon}\rangle$ for the HDMS treated sample set 2. Solid and dashed lines represent the DRIE and RIE method, respectively.

4.2.6 Set 3

4.2.6.1 HF

The measurement of Q_i as a function of $\langle n_{photon} \rangle$ for the HF sample with PTFE surface passivation of device set 3 is shown in Fig. 4.11. The Q_is of the DRIE and RIE resonators are now more grouped, where all DRIE resonators, except resonator 3, have higher internal quality factors at low power than the RIE resonators. The best performing resonator has a Q_i of $1.84{\cdot}10^6$ at single-photon level.

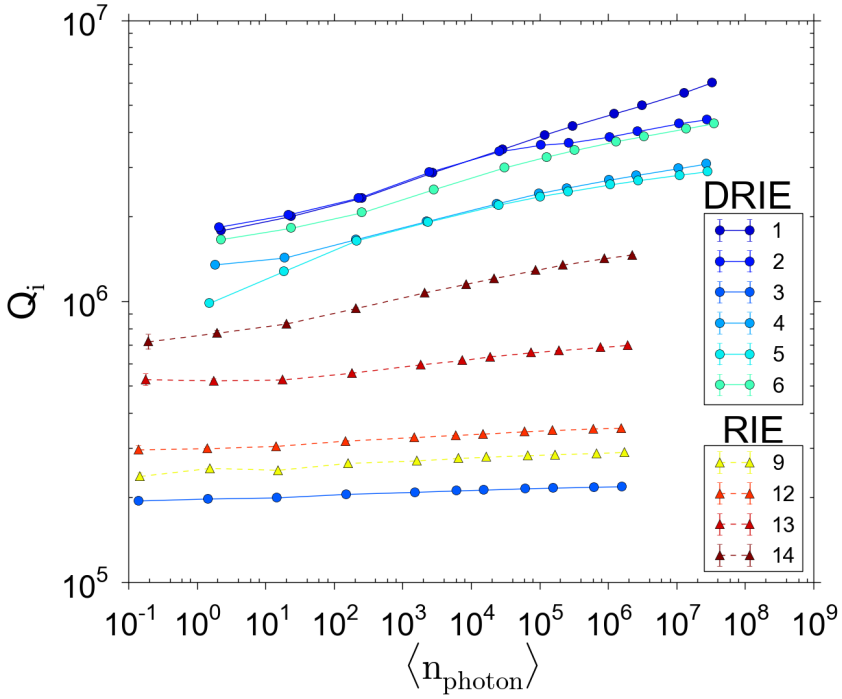

Figure 4.11: Q_i as a function of $\langle n_{photon} \rangle$ for the HF treated sample of device set 3. Solid and dashed lines represent the DRIE and RIE method, respectively.

4.2.6.2 HDMS

Comparable to HF set 3, the resonators of the HDMS treated sample is shown in Fig. 4.12 are more grouped and with a larger difference in Q_i between DRIE and RIE resonators, with the exception of resonator 3. The best performing resonator is DRIE resonator 5 with a Q_i of $1.84{\cdot}10^6 \pm 4.2{\cdot}10^4$ at single-photon level.

For the lowest $P_{in}$the RIE resonators do not have a sudden drop in $Q_i$as they did for HDMS set 2. The Q_i for RIE resonators of set 3 is also less power dependent than the same ones for set 2.

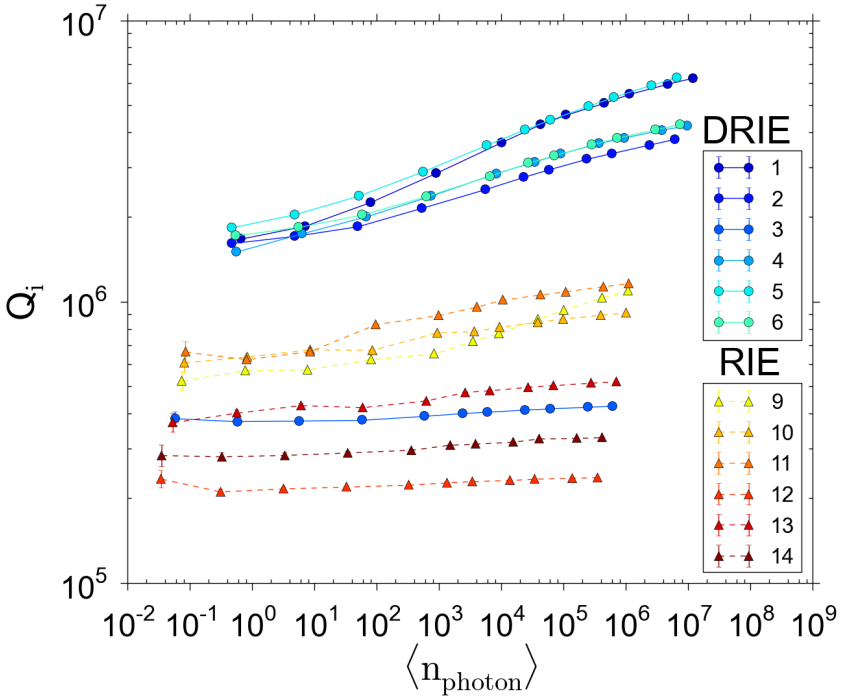

Figure 4.12: Q_i as a function of $\langle n_{photon} \rangle$ for the HDMS treated sample of device set 3. Solid and dashed lines represent the DRIE and RIE method, respectively.

Chapter 5

Discussion

5.1 HDMS DRIE over time

The DRIE resonators of HDMS set 1 have performed better than the RIE resonators, but it has been observed that the Q_i of these resonators changed with switching fridges. Specifically, the Q_i for the DRIE resonators of HDMS set 1 in laFerrari were not as high as the first time in laVespa and the Q_i measurement the second time in laVespa(2) was lower than in laFerrari. Between the first time in laVespa and the cooldown in laFerrari the sample was for $\sim$1 month in contact with air. From laFerrari to laVespa(2) the sample was kept in vacuum as much as possible. A graph of the time dependent degradation of the performance of HDMS DRIE resonators is shown in Fig. 5.1. The decrease in Q_i could be explained by the oxidation of the side walls during the time in air. The power dependence of Q_i for the DRIE resonators in laVespa(2) has vanished completely and no cause for that has been found.

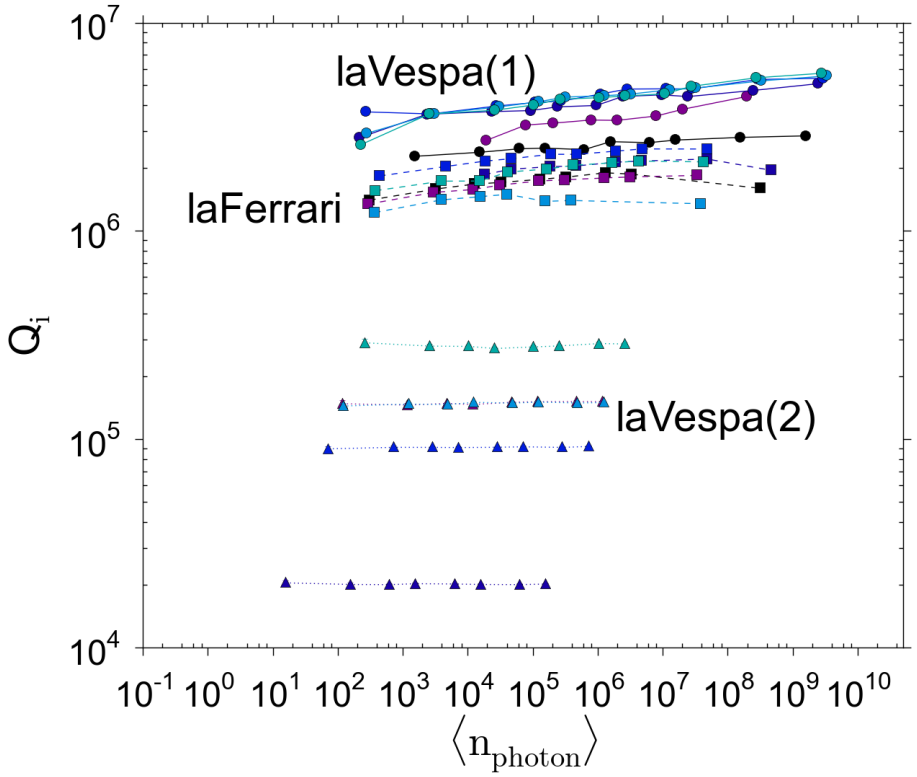

Figure 5.1: Q_i as a function of $\langle n_{photon} \rangle$ for the HDMS treated sample of device set 1 for measurements subsequently in laVespa, laFerrari and laVespa(2), represented by the solid, dashed and dotted lines, respectively. Note that the measurement in laFerrari has been done at ∼20 mK and in laVespa at ∼250 mK.

5.1.1 HF vs. HDMS

So far the DRIE resonators have a tendency of outperforming the RIE resonators with $Q_i > 10^6$, therefore it is useful to plot the HF DRIE and HDMS DRIE together in one graph to differentiate between the performance of resonators when treated with HF or HDMS. This is done for set 2 in Fig. 5.2 and set 3 in Fig. 5.3. Set 2 resonators on the HDMS sample show a stronger power dependence than those on the HF treated sample, but at the same time the Q_i is higher, both for single photon level as for high $\langle n_{photon} \rangle$. The larger decrease in Q_i when moving into sub single photon regime results suggests two-level fluctuators to be the dominant source of losses.

Surface passivation with PTFE of set 3 samples seems to decrease the difference in over-

all Q_i between HF and HDMS treated samples as it increases the performance of the HF treated resonators, as shown in Fig. 5.3. At the same time set 3 does not produce the highest Q_i measured of all samples so far. The *highest* Q_i at single photon level is reached by HDMS DRIE resonator 1 on the unpassivated set 2 with Q_i=2.24·10^6±1.34·10^5.

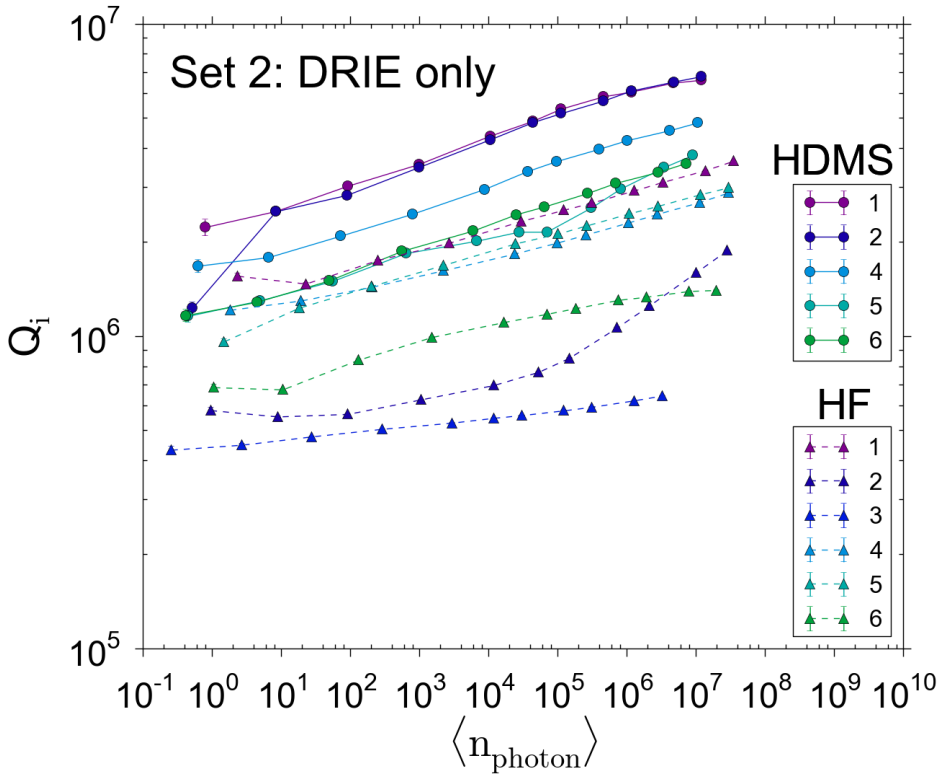

Figure 5.2: Q_i as a function of $\langle n_{photon} \rangle$ for the DRIE resonators of HF and HDMS treated sample set 2. Solid and dashed lines represent the resonators of the HDMS and HF treated samples, respectively.

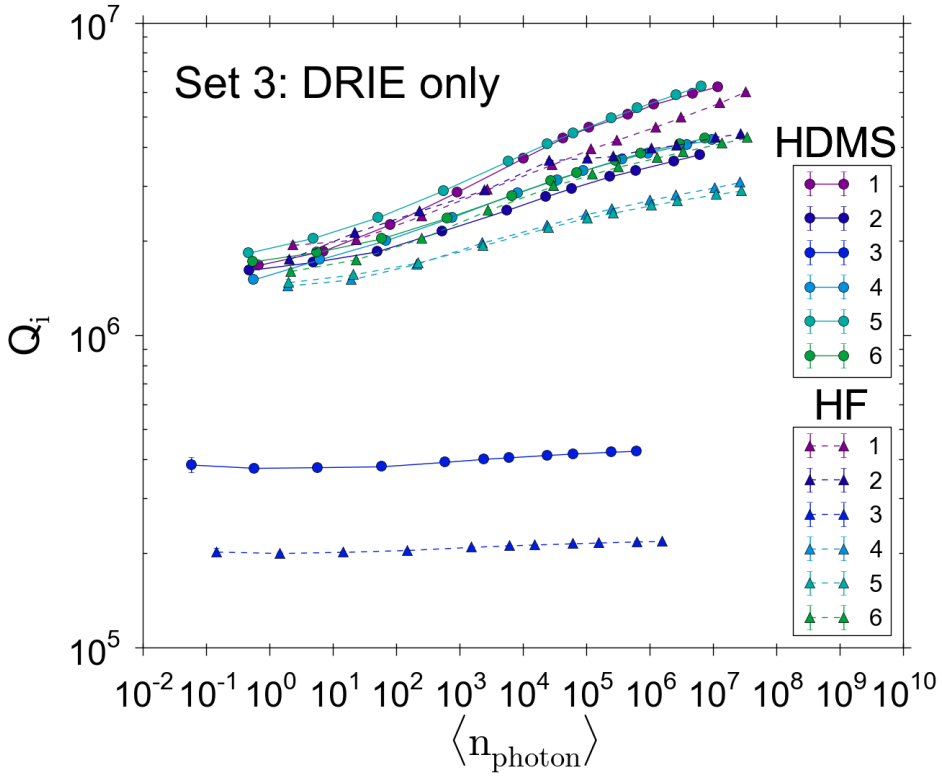

Figure 5.3: Q_i as a function of $\langle n_{photon} \rangle$ for the DRIE resonators of HF and HDMS treated sample set 3. Solid and dashed lines represent the resonators of the HDMS and HF treated samples respectively.

5.2 Fridge comparison

For HDMS treated samples of set 3 it was decided to compare the performance of the resonators in the fridges laFerrari and laVespa, which operate at a T_{base} of ∼20 mK and ∼250 mK, respectively. We are mostly interested in DRIE resonators because of their higher Q_is, these are therefore shown in Fig. 5.4 for both laFerrari and laVespa. The resonators when measured in laVespa perform slightly better than in laFerrari at low power and vice versa at high power. The Q_i at single photon level is lower in laFerrari since the energy absorption by TLS is less at ∼250mK than at ∼20mK, because of TLS saturation. Still, the error of the measurement in laVespa is higher due to higher noise levels than in comparison to laFerrari, 80K and 2.5K, respectively. Taking these differences into account, we validated the laVespa as being a viable and quick substitute for laFerrari when performing Q_i measurements.

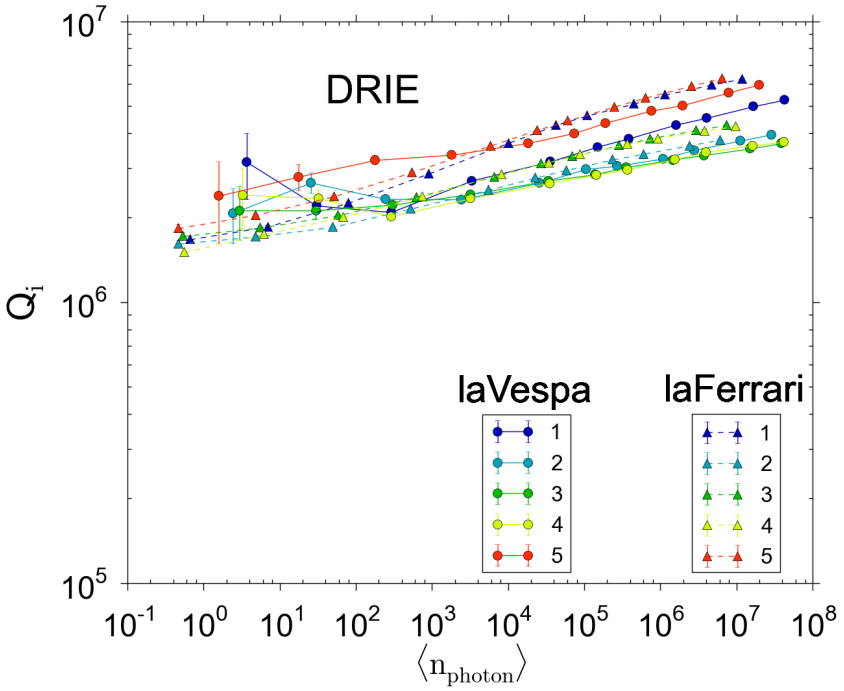

Figure 5.4: Q_i as a function of $\langle n_{photon} \rangle$ for the DRIE resonators of HDMS treated sample set 3 for measurements in laFerrari and laVespa. Solid and dashed lines represent the resonators measured at ∼20 mK and ∼250 mK, respectively.

Chapter 6

Conclusions

Three sets of CPW resonators have been fabricated, each of them consisting of two samples which surfaces were treated with either HF or HDMS method. The resonators have been etched using both RIE and DRIE.

Comparison of both HF and HDMS treated samples of set 2 and 3 consistently showed higher Q_i for DRIE resonators over RIE, which suggests a reduced influence of lossy TLS at the substrate-air interfaces, due to the recessed interface. The DRIE resonators of the HDMS treated sample of set 1 and 2 have higher Q_i than the resonators of the HF treated sample of the same set. The *highest* Q_i at single photon level is reached by a HDMS DRIE resonator of set 2 with Q_i=$2.24{\cdot}10^6{\pm}1.34{\cdot}10^5$ at f_0=4.16 GHz. Thus, using HDMS treatment for changing the metal-substrate interface suggests a localized reduction of TLS density.

Further research is encouraged to explore the variation of the DRIE process, as the influence of trench depth, underetch and sidewall roughness, is still not thoroughly understood. In light of this, it seems plausible that further improvements of Q_i can be achieved. Furthermore, the degradation in Q_i over time for the HDMS treated sample requires further investigation and whether or not PTFE sidewall passivation prevents any Q_i degradation.

Most important of all, the fabrication of a transmon qubit using the techniques described in this thesis is encouraged. It would be of tremendous relevance if such a qubit has longer relaxation times than the current state of the art transmon qubits, which have T_1 of the order of 10-15 µs. In fact, from the highest Q_i at single-photon level it can be estimated that a transmon qubit etched using DRIE would have $T_1 \sim 80$ µs.

Appendix A

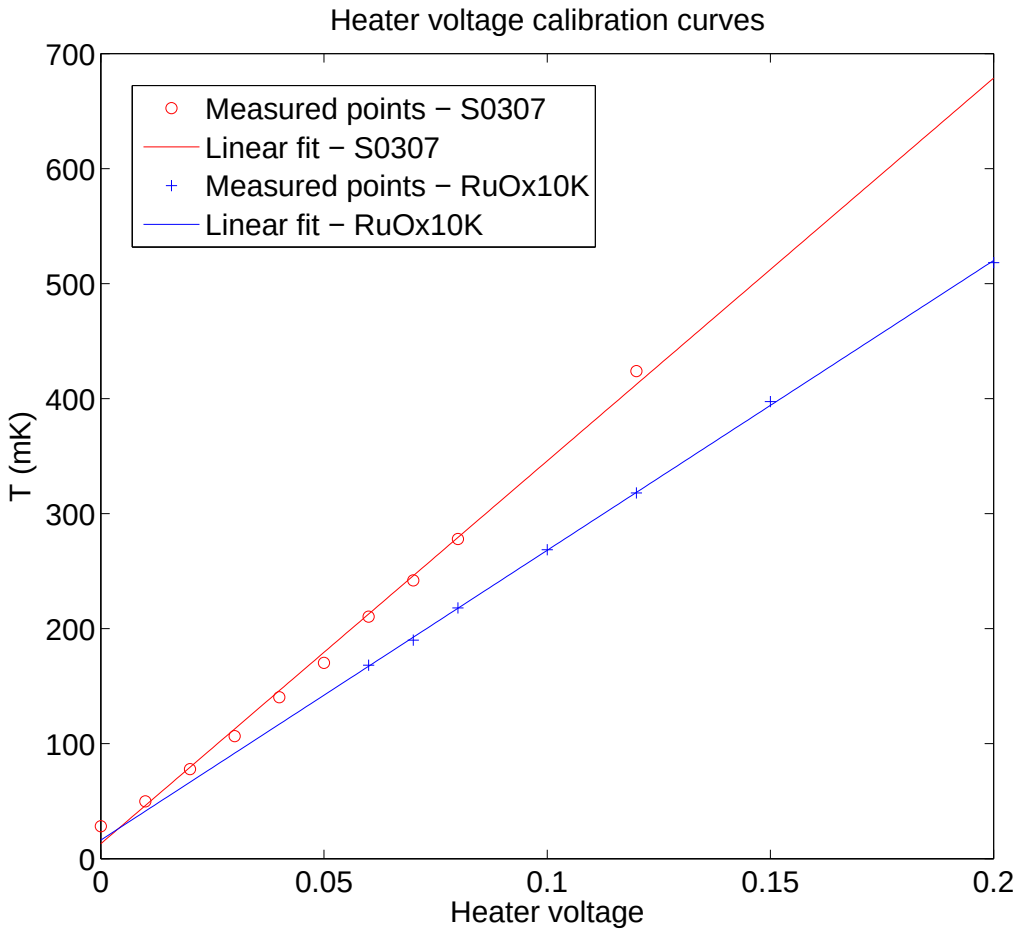

Figure A.1: Calibration curves of two thermometers used separately in the balls mounted in the laFerrari fridge. The RuOx10K is calibrated with its standard calibration curve, resulting in a temperature measurement as shown. Following its temperature-resistance calibration curve this thermometer is considered not well calibrated for T¡150 mK. At the same time, the S0307 thermometer is not well calibrated for T¿150 mK.

Bibliography

[1] M. Shakori. Accurate fabrication of the transmon qubit. BEP report, Delft University of Technology, 2011.

[2] A. Wallraff, D.I. Schuster, A. Blais, L. Frunzio, R.S. Huang, J. Majer, S. Kumar, S.M. Girvin, and R.J. Schoelkopf. Strong coupling of a single photon to a superconducting qubit using circuit quantum electrodynamics. *Nature*, 431:162–167, 2004.

[3] K. Geerlings, S. Shankar, E. Edwards, L. Frunzio, R.J. Schoelkopf, and M.H. Devoret. Improving the quality factor of microwave compact resonators by optimizing their geometrical parameters. *Appl. Phys. Lett.*, 100(19):192601, 2012.

[4] A. Megrant, C. Neill, R. Barends, B. Chiaro, Y. Chen, L. Feigl, J. Kelly, E. Lucero, M. Mariantoni, P.J.J. OMalley, et al. Planar superconducting resonators with internal quality factors above one million. *Appl. Phys. Lett.*, 100(11):113510, 2012.

[5] J. Gao, M. Daal, A. Vayonakis, S. Kumar, J. Zmuidzinas, B. Sadoulet, B.A. Mazin, P.K. Day, and H.G. Leduc. Experimental evidence for a surface distribution of two-level systems in superconducting lithographed microwave resonators. *Appl. Phys. Lett.*, 92(15):152505–152505, 2008.

[6] R. Barends, N. Vercruyssen, A. Endo, P.J. De Visser, T. Zijlstra, T.M. Klapwijk, P. Diener, S.J.C. Yates, and J.J.A. Baselmans. Minimal resonator loss for circuit quantum electrodynamics. *Appl. Phys. Lett.*, 97:023508, 2010.

[7] J.M. Sage, V. Bolkhovsky, W.D. Oliver, B. Turek, and P.B. Welander. Study of loss in superconducting coplanar waveguide resonators. *J. Appl. Phys.*, 109(6):063915, 2011.

[8] D.S. Wisbey, J. Gao, M.R. Vissers, F.C.S. da Silva, J.S. Kline, L. Vale, and D.P. Pappas. Effect of metal/substrate interfaces on radio-frequency loss in superconducting coplanar waveguides. *J. Appl. Phys.*, 108(9):093918, 2010.

[9] A.D. OConnell, M. Ansmann, R.C. Bialczak, M. Hofheinz, N. Katz, E. Lucero, C. McKenney, M. Neeley, H. Wang, E.M. Weig, et al. Microwave dielectric loss at single photon energies and millikelvin temperatures. *Appl. Phys. Lett.*, 92(11):112903, 2008.

[10] J. Wenner, R. Barends, R.C. Bialczak, Y. Chen, J. Kelly, E. Lucero, M. Mariantoni, A. Megrant, P.J.J. OMalley, D. Sank, et al. Surface loss simulations of superconducting coplanar waveguide resonators. *Appl. Phys. Lett.*, 99(11):113513, 2011.

[11] P. de Visser. *Quasiparticle dynamics in aluminium superconducting microwave resonators*. PhD thesis, TU Delft, 2014.